Geophys. J. Int. (2008) **173,** 718–732 doi: 10.1111/j.1365-246X.2008.03754.x

A deep crustal fluid channel into the San Andreas Fault system near Parkfield, California

M. Becken,[1] O. Ritter,[1] S. K. Park,[2] P. A. Bedrosian,[3] U. Weckmann[1,4] and M. Weber[1,4]

[1] *GeoForschungsZentrum Potsdam, Geophysical Deep Sounding, Telegrafenberg,* 14473 *Potsdam, Germany. E-mail: becken@gfz-potsdam.de*
[2] *University of California Riverside, Department of Earth Sciences,* 2207 *Geology, Riverside,* CA 92521*, USA*
[3] *US Geological Survey, MS* 964, *Box* 25046, *Bldg* 20, *Denver,* CO 80225*, USA*
[4] *University Potsdam, Department of Geosciences, Karl-Liebknecht-Strasse* 24, *Haus* 27, 14476 *Potsdam, Germany*

Accepted 2008 January 12. Received 2008 February 25; in original form 2007 June 18

SUMMARY

Magnetotelluric (MT) data from 66 sites along a 45-km-long profile across the San Andreas Fault (SAF) were inverted to obtain the 2-D electrical resistivity structure of the crust near the San Andreas Fault Observatory at Depth (SAFOD). The most intriguing feature of the resistivity model is a steeply dipping upper crustal high-conductivity zone flanking the seismically defined SAF to the NE, that widens into the lower crust and appears to be connected to a broad conductivity anomaly in the upper mantle. Hypothesis tests of the inversion model suggest that upper and lower crustal and upper-mantle anomalies may be interconnected. We speculate that the high conductivities are caused by fluids and may represent a deep-rooted channel for crustal and/or mantle fluid ascent. Based on the chemical analysis of well waters, it was previously suggested that fluids can enter the brittle regime of the SAF system from the lower crust and mantle. At high pressures, these fluids can contribute to fault-weakening at seismogenic depths. These geochemical studies predicted the existence of a deep fluid source and a permeable pathway through the crust. Our resistivity model images a conductive pathway, which penetrates the entire crust, in agreement with the geochemical interpretation. However, the resistivity model also shows that the upper crustal branch of the high-conductivity zone is located NE of the seismically defined SAF, suggesting that the SAF does not itself act as a major fluid pathway. This interpretation is supported by both, the location of the upper crustal high-conductivity zone and recent studies within the SAFOD main hole, which indicate that pore pressures within the core of the SAF zone are not anomalously high, that mantle-derived fluids are minor constituents to the fault-zone fluid composition and that both the volume of mantle fluids and the fluid pressure increase to the NE of the SAF. We further infer from the MT model that the resistive Salinian block basement to the SW of the SAFOD represents an isolated body, being 5–8 km wide and reaching to depths >7 km, in agreement with aeromagnetic data. This body is separated from a massive block of Salinian crust farther to the SW. The NE terminus of resistive Salinian crust has a spatial relationship with a near-vertical zone of increased seismic reflectivity $\sim$15 km SW of the SAF and likely represents a deep-reaching fault zone.

Key words: Magnetotelluric; Transform faults; Crustal structure.

1 INTRODUCTION

Fluids are ultimately linked to many fault-related processes at transform plate boundaries. Fault zone fluids at high pressures can lower the effective normal stress on a fault and decrease its shear strength at seismogenic depths (Hardebeck & Hauksson 1999). Overpressured fluids within the core of the San Andreas Fault (SAF) were considered a likely explanation for its weakness (Zoback 2000) between Parkfield and Hollister, CA, where the SAF exhibits a combination of aseismic creep and repeating micro-earthquakes. Directly accessing fluids and understanding their role and the *in situ* physical and chemical conditions within the core of the SAF is one of the major goals of the San Andreas Fault Observatory at Depth (SAFOD) (Hickman *et al.* 2004).

From the chemical analysis of well waters, Kennedy *et al.* (1997) proposed that fluids can enter the brittle regime of the SAF system from the lower crust and mantle and may contribute directly to fault-weakening high fluid pressures at seismogenic depths. In this

scenario, the brittle–ductile transition appears at least episodically as a permeable boundary and fault-weakening fluid pressures would be generated by high flux of deep crustal or mantle fluids that are supplied to the seismogenic zone from the ductile lower crust at superhydrostatic pressures.

Recent studies within the SAFOD main hole north of Parkfield indicate that pore pressures within the core of the SAF are not anomalously high (Zoback *et al.* 2006) and that mantle-derived fluids are minor contributors to the fault-zone fluid composition (Wiersberg & Erzinger 2007). However, both the fluid pressure and the amount of mantle-derived fluids appear to increase northeastward within the North American Plate (Wiersberg & Erzinger 2007). This suggests that the seismically defined SAF is not a major channel for deep-rooted fluid ascent—at least at the drilled depths—and that alternative pathways must exist.

Equally important are the physical properties of the crust surrounding the seismogenic fault, as rheological variability within the fault-surrounding country rock may strongly control the location of the fault and its mechanical behaviour. For instance, within the transpressive regime of the SAF, transform motion near Parkfield is accommodated primarily by the SAF, while thrusting and backthrusting accommodates compressional stress farther to the NE towards the town of Coalinga (Guzofski *et al.* 2007). Modelling of the thrusting regime between Parkfield and Coalinga suggests that fluid pressure release within the thrusting regime may mediate the earthquake cycle at the SAF (Miller 1996). This indicates, that accommodation of transform motion (primarily at the SAF) and compressional strain (farther to the NE) are coupled processes extending over a wider region than implied by the narrow zone of seismicity.

Magnetotelluric (MT) imaging of the subsurface can provide important constraints on the crustal fluid distribution and hence on the mechanical and dynamic state of the SAF system. The presence of fluids within pores affects the electrical conductivity of rocks (Gueguen & Palciauskas 1994). Small amounts of brine, when interconnected, can increase the bulk rock conductivity of an entire subsurface region by several orders of magnitude (Jones 1992). The MT method is the only geophysical technique capable of probing the Earth's deep interior at crustal- and upper-mantle scales for its electrical conductivity structure.

Previous MT investigations across the central SAF revealed zones of high electrical conductivity in the upper 2 km of the Earth's crust (Unsworth *et al.* 1997, 2000; Bedrosian *et al.* 2004). Fluids of meteoric or metamorphic origin, circulating in fault-related fracture zones, were suggested as the cause of the high conductivity. These electrical conductivity images played an important role in pin-pointing the location of the SAFOD site near Parkfield, CA.

Here, we report on new MT data collected in 2005 as a joint initiative between the GeoForschungsZentrum Potsdam and the University of California Riverside. We acquired MT data at 43 broad-band stations and 12 combined long-period/broad-band stations along a 45-km-long profile across the SAF near the SAFOD (black line labelled MT profile in Fig. 1). This MT profile is coincident with the seismic reflection/refraction line of Hole *et al.* (2006). An additional 33 combined long-period/broad-band stations are distributed in an area of $50 \times 50\,\mathrm{km}^2$ (see Fig. 1).

In this paper, we concentrate on the 2-D interpretation of the profile MT data. Our data were complemented with 11 broad-band sites of the northernmost profile of previous shallower investigations (Line 1 in Unsworth *et al.* 2000). This paper is organized as follows: After a brief introduction to the MT method and an overview about the new MT data, we show in Section 2.2 that a 2-D approach is adequate to explain most of the features of the profile data and that the geoelectric strike corresponds well with the predominant geological strike (NW). We further describe how we handle data with 3-D effects prior to 2-D inversion (see Section 2.3). Crustal resistivity models inferred from the MT data are presented and evaluated in Section 3 and discussed in Section 4, in particular with respect to the crustal fluid distribution.

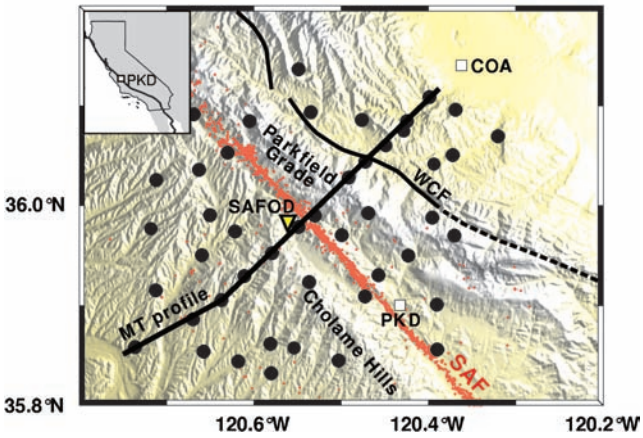

Figure 1. Site map. Emphasis for this paper is on the MT data recorded at 66 sites along a 45-km-long profile (solid black line), centred on the SAFOD site (yellow triangle). This profile includes 11 sites from a previous MT survey (Unsworth *et al.* 2000) in its central part. Solid black circles indicate site locations of additional long-period/broad-band recordings in array configuration. Red dots indicate the seismicity along the SAF (Thurber *et al.* 2006). PKD Parkfield; COA Coalinga; WCF Waltham Canyon Fault; inset shows a map of California, the SAF and the location of Parkfield.

2 MT DATA AND DATA ANALYSIS

2.1 MT data

MT makes use of natural electromagnetic field variations to probe the subsurface conductivity structure. The MT data are frequency-dependent, complex-valued 2×2 impedance tensors $\mathbf{Z}$ and 1×2 vertical magnetic transfer functions $\mathbf{T}$. They represent the inductive response of a conducting subsurface to an external time-varying magnetic field and are defined via the linear relations $\mathbf{E}_h = \mathbf{Z}\mathbf{H}_h$ and $H_z = \mathbf{T}\mathbf{H}_h$ in the spectral domain, where subscripts h and z denote horizontal and vertical components of the electric and magnetic field vectors $\mathbf{E}$ and $\mathbf{H}$, respectively. The frequency f (or its reciprocal period T) of the inducing fields can be viewed as a rough (non-linear) proxy for depth, as lower frequencies penetrate deeper into the subsurface (skin-depth effect). Inverse modelling of a number of sites and a range of periods simultaneously is employed to extract the subsurface conductivity structure embodied in the MT data.

$\mathbf{Z}$ and $\mathbf{T}$ were statistically estimated from orthogonal observations of time-varying horizontal electric and three-component magnetic field recordings at the Earth's surface, using a combination of the robust remote-reference processing of Egbert & Booker (1986) and the robust code of Ritter *et al.* (1998) and Weckmann *et al.* (2005). In the field setup the magnetic sensors and the electric field dipoles were aligned in geomagnetic coordinates, corresponding to a declination of N14°E in central California. When applying coordinate transforms, we refer to the geomagnetic system; positive rotation angles correspond to clockwise rotation from geomagnetic north. Strike directions are expressed in geographic coordinates. The strike

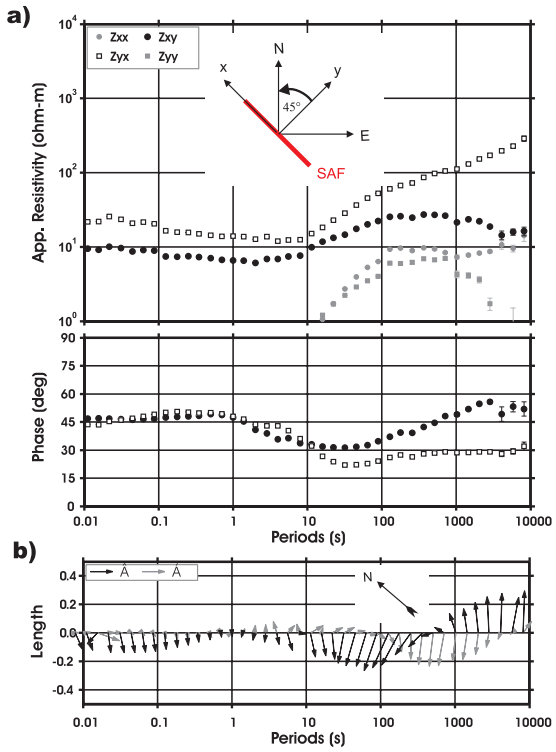

Figure 2. MT data of site 20, located 1 km to the NE of the SAF. (a) Apparent resistivities and phases (upper and middle panel) and (b) induction vectors (lower panel) represent the impedance tensor and the vertical magnetic TF. Statistical error bars of impedances are at most periods smaller than the symbol size; error bars on the induction vectors have been omitted for clarity. The coordinate system used to depict apparent resistivities and phases is rotated to N45°W, that is, the *y*-axis is in the profile direction and the *x*-axis is aligned with the SAF (see inset). Induction vectors are depicted in (rotated) map view so that the upward direction is along the profile (see north arrow). Real induction vectors (black arrows, Wiese convention) are predominantly oriented perpendicular to the SAF (SW at short periods and NE at long periods), indicating a geoelectric strike direction aligned with the SAF. Grey arrows indicate imaginary induction vectors.

direction of the SAF near Parkfield is approximately N45°W, corresponding to −59° from geomagnetic north.

At a particular frequency, the impedance elements Z_{ij} are converted into an apparent resistivity ($\rho_{a,ij} = |Z_{ij}|^2/5f$) and a phase $\phi_{ij} = \arg Z_{ij}$. Induction vectors are vectorial representations of **T** (Wiese 1962) in map view. Fig. 2 shows the MT data at site 20, located 1 km to the NE of the SAF. We use this site as an example to illustrate subsequent steps of data analysis. The coordinate system used to depict apparent resistivities and phases in Fig. 2(a) is rotated to the strike of the SAF (−59°; corresponding to N45°W), that is, the *x*-axis is aligned with the SAF (see inset of Fig. 2) and the *y*-axis is in the profile direction (*z* is positive downwards).

In order to properly depict the induction vectors in Fig. 2(b), we rotated the map view by −45° (see north arrow). In this representation, induction vectors point predominantly upwards and downwards corresponding to orientations in the NE and SW direction, respectively. In other words, the induction vectors at this site are predominantly oriented perpendicular to the SAF.

In Section 2.2, we demonstrate that a 2-D approach ($\rho = \rho(y, z)$) with a strike direction of N42.5°W is adequate to model our data. Under 2-D conditions, the MT data separate into two distinct, orthogonal polarizations: the E- and the H-polarization. The presumed

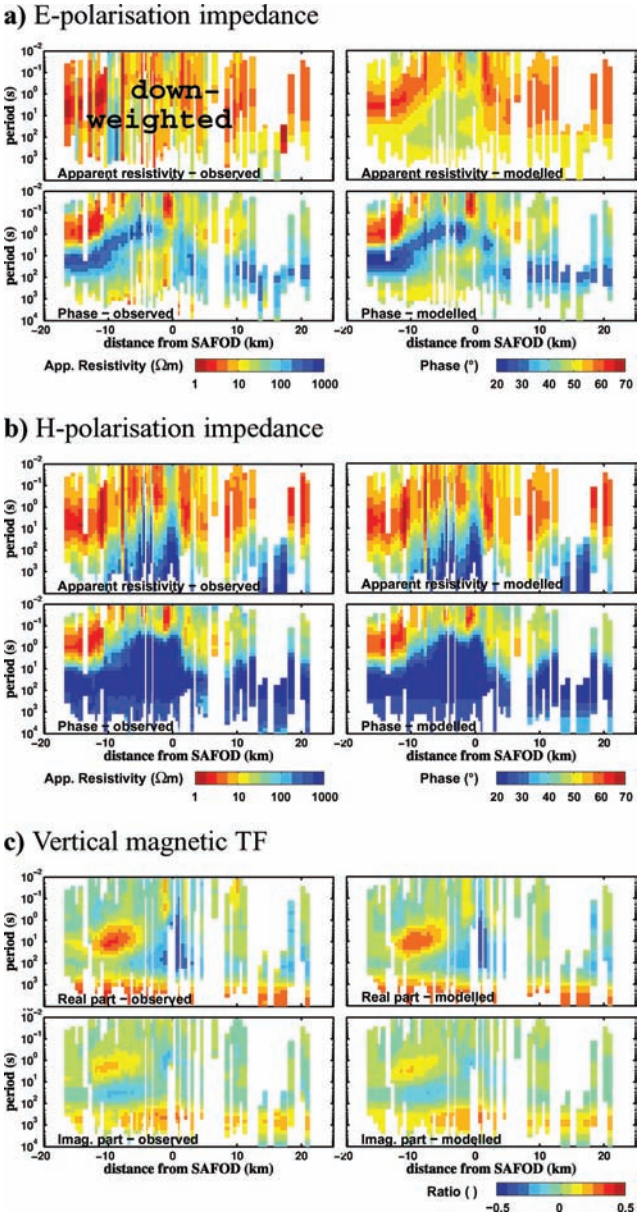

Figure 3. MT pseudo-sections of measured data rotated into the strike direction N42.5°W (left-hand panels) and data predicted from the final 2-D model shown in Figures 9a (middle panel) and 11. See text for details.

E- and H-polarization impedances (Z_{xy} and Z_{yx}, respectively) and the vertical magnetic transfer functions (T_y) of the entire data set are depicted as pseudo-sections in the left-hand panels of Fig. 3; these quantities represent the observed data rotated by −56.5° (counterclockwise) into the geoelectric strike. White areas in Fig. 3 correspond to missing data or obvious outliers which were removed manually. Pseudo-sections in the right-hand panels of Fig. 3 correspond to the predicted response of our final 2-D model (see Section 3.5).

E- and H-polarization correspond to tangential and normal current flow, respectively, with respect to the geo-electric strike direction. As a consequence, the MT responses for the two polarizations exhibit different sensitivities to the subsurface resistivity structure, and it is difficult to interpret data pseudosections in terms of a subsurface resistivity distribution. In particular, the penetration depth at a particular period can vary along the profile and differ for the

E- and H-polarizations. With this in mind, the properties of the measured data are briefly characterized as follows: at short periods both E- and H-polarization impedances indicate low resistivities near-surface. At longer periods, H-polarization apparent resistivities and phases indicate increased resistance for across-strike currents, while the E-polarization data indicate laterally variable resistance along the profile for deep along-strike currents. In particular, phases $>45^\circ$ are observed at profile distances <0 km (SW of SAFOD) for periods >10–100 s and indicate the presence of a high-conductivity zone at corresponding depths and distances. In this region and period range, a prominent positive and negative vertical magnetic field anomaly is observed (orange and blue colours in Fig. 3c) which indicates a deep lateral resistivity contrast. At periods $\sim$1000 s, another vertical magnetic field anomaly is evident in the real part of T_y at all sites. We attribute this anomaly to the effect of the Pacific ocean.

2.2 Dimensionality, strike and galvanic distortion analysis

As mentioned before, both real and imaginary induction vectors at site 20 (Fig. 1, lower panel) are predominantly parallel to the profile and perpendicular to the SAF, consistent with 2-D conditions. Diagonal impedances, however, do not vanish at this site (and at the other sites) and indicate the presence of 3-D effects. With so-called tensor decomposition schemes it can be tested whether 3-D effects are caused by a large scale 2-D regional structure with some local 3-D distortions or if the underlying structure is 3-D on a regional scale (Bahr 1988; Groom & Bailey 1989).

If 3-D effects are due to local small-scale heterogeneities, a real, frequency-independent distortion matrix **D** can be separated from the impedance tensor data to recover the regional 2-D impedance. Let the regional impedance be denoted as $\mathbf{Z}^{reg}$, then the measured impedance is $\mathbf{Z} = \mathbf{D}\mathbf{R}^T(\delta)\mathbf{Z}^{reg}\mathbf{R}(\delta)$. Here, **D** describes a rotation and amplification (static shift) of the regional electric field components due to galvanic distortion (e.g. Smith 1995), **R** is the 2-D clockwise rotation matrix and δ is the regional strike direction; superscript T denotes matrix transpose. Since the amount of static shift, being expressed in an offset of apparent resistivity curves, can not be resolved with any of the decomposition techniques (e.g. Caldwell *et al.* 2004), the so-called gain factors are set to unity. For the impedance tensor analysis, we make use of the decomposition scheme of Becken & Burkhardt (2004), which infers the existence of a regional 2-D structure and the geoelectric strike direction from an ellipse parametrization of the impedance tensor columns. The ellipticities (ϵ_x and ϵ_y) of the impedance tensor columns are rotationally variant; they vanish in case of 2-D conditions if the data are rotated to the regional strike. Hence, in order to determine the strike direction, we minimize the sum of squared ellipticities weighted with their variances by rotating the coordinate system. The minimization is applied for a range of periods (and sites) simultaneously to improve the stability of the solution, similar to the multiperiod multisite approach of McNeice & Jones (2001).

For site 20, we determine a rotation angle of -59°. The ellipticities of the rotated impedance tensor columns are depicted in the upper panel of Fig. 4. They vanish within their confidence intervals at all periods except for the range between 5 and 100 s, where values of up to 0.1–0.2 are reached. The weighted averages of ellipticties over all periods at site 20 are $\overline{\epsilon}_x = 0.02 \pm 0.05$ and $\overline{\epsilon}_y = -0.03 \pm 0.07$, that is, they are close to zero. From our experience, ellipticities of strong 3-D data can exceed values >1; moderate ellipticities <0.15–0.2 are still predominantly consistent with 2-D conditions. In comparison, the phase-sensitive skew (Bahr 1988) at site 20 is less than 0.25 at all periods; skew-values below 0.3 are often considered to be consistent

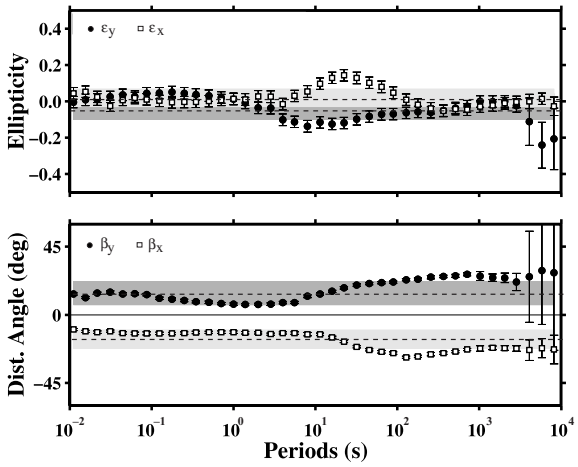

Figure 4. Ellipse parameters of the impedance columns for site 20 (see Fig. 2). Ellipticities are shown in the upper panel and distortion angles, that is, the rotation of electric field components away from the regional coordinate axes, in the lower panel. Dashed lines indicate weighted averages; the width of grey patches corresponds to the weighted rms deviation of mean ellipse parameters. The data are rotated by -59°W to the geoelectric strike direction estimated for the entire period range. In rotated coordinates, the ellipticities vanish at long and at short periods (for $T < 3$ s and $T > 100$ s) and are in agreement with regional 2-D conditions. At intermediate periods ($\sim$5–100 s), however, moderate 3-D effects are indicated by the non-vanishing ellipticities. The distortion angles, depicted in the lower panel, are constant over the respective period ranges of vanishing ellipticities, but change at intermediate periods.

with a 2-D approach. We conclude from this that site 20 exhibits predominantly 2-D characteristics (striking at N45°W with a 90° ambiguity that cannot be resolved from MT impedance data alone) with some moderate 3-D effects at intermediate periods. The 90° impedance tensor strike ambiguity can be resolved in conjunction with the induction vectors, that point perpendicular to strike in 2-D conditions (in the Wiese convention used here, real induction vectors point away from conductive zones). The induction vectors at site 20 (*cf.* Fig. 2) clearly indicate a strike direction aligned with the SAF (N45°W).

Under regional 2-D conditions, the orientations of ellipses with respect to rotated coordinates correspond to the rotation of the principal electric field due to galvanic distortion (Becken & Burkhardt 2004); they are denoted as the distortion angles β_x and β_y and correspond to the distortion angles of Smith (1995). Conditions for regional two-dimensionality require also that the distortion angles at each site are constant over period. Within the same intermediate period range, where ellipticities indicate moderate 3-D effects, the distortion angles (lower panel in Fig. 4) change by 5–10°, while they are approximately constant over the short- and long-period range where the ellipticities vanish. The weighted averages of distortion angles over the entire period range are $\overline{\beta}_x = -16.4^\circ \pm 6.1^\circ$ and $\overline{\beta}_y = 14.8^\circ \pm 7.6^\circ$ (dashed line and grey patches).

Assuming for the moment that the data were truly 2-D on a regional scale afflicted with local 3-D distortion, we reconstruct the distortion matrix **D** from the weighted means of β_x and β_y over period. Then, the rotation of the electric field components due to galvanic distortion can be reversed in order to retrieve the regional impedance tensor $\mathbf{Z}^{reg} = \mathbf{D}^{-1}\mathbf{R}\mathbf{Z}\mathbf{R}^T$. A relatively large uncertainty in the distortion model parameters estimated over all periods is expressed in large rms deviations from their weighted averages ($\overline{\beta}_x = -16.4^\circ \pm 6.1^\circ$ and $\overline{\beta}_y = 14.8^\circ \pm 7.6^\circ$) and

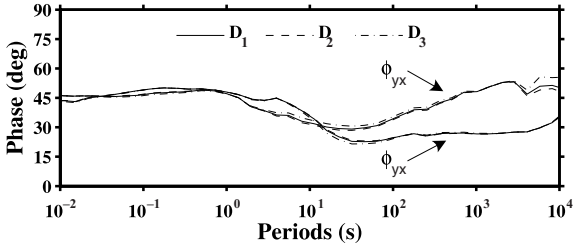

Figure 5. Phases of the regional impedance tensor at site 20, using three different distortion models: $\mathbf{D}_1$ is determined from the weighted average of the distortion angles over the entire period range; models $\mathbf{D}_2$ and $\mathbf{D}_3$ are determined from weighted averages over the period ranges $T = 0.01$–3 s and $T = 100$–10 000 s, respectively (see text). The differences between the regional phases using these distortion models is small, and closely resembles the distorted phases.

raise the question of their usefulness. We test the importance of decomposing the data by incorporating three different distortion models: model $\mathbf{D}_1$ is determined from the weighted average of the distortion angles over the entire period range (see above), while models $\mathbf{D}_2$ ($\overline{\beta}_x = -11.8 \pm 0.7^\circ$ and $\overline{\beta}_y = 10.4 \pm 3.0^\circ$) and $\mathbf{D}_3$ ($\overline{\beta}_x = -25.1 \pm 2.4^\circ$ and $\overline{\beta}_y = 10.4 \pm 2.2^\circ$) are determined from weighted averages over the period ranges $T = 0.1$–3 s and $T = 100$–10 000 s; that is, the period ranges most closely resembling 2-D conditions. Note that the distortion models $\mathbf{D}_2$ and $\mathbf{D}_3$ are estimated with a much higher certainty.

Fig. 5 compares the effect of these three different distortion models on the off-diagonal phases of the regional impedance tensor at site 20 (rotated to strike). Obviously, the differences are very small and are only visible within the intermediate period range, where moderate 3-D effects are evident. As the variation of regional phases is within the error bars of the observed (and distorted) phases we use the rotated tensor elements directly instead of making use of a distortion model. This means that we effectively use the tensor decomposition only to determine the best-fitting strike direction.

Site 20 is representative of the entire data set in terms of dimensionality and rotational properties of the impedance tensor. Fig. 6(a) shows a rose diagram of strike directions, estimated with the above described tensor decomposition scheme for each site separately and

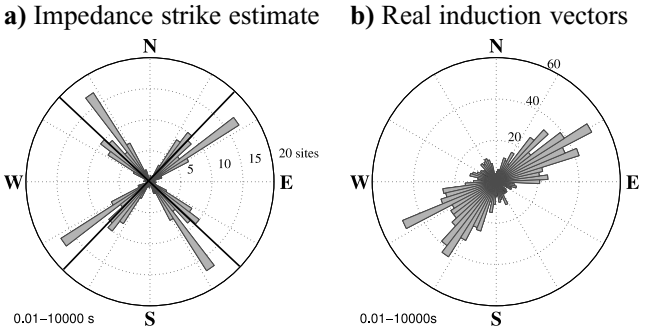

Figure 6. Rose diagrams of directional parameters. (a) Cumulative geoelectric strike directions obtained from impedance tensor analysis (with a 90° ambiguity). Geoelectric strike angles cluster at N40° W ± 5°. The solid black line is derived from a multiperiod, multisite optimization using all sites and periods; it indicates a strike direction of N42.5° W. (b) Cumulative orientations of real induction vectors using all periods; imaginary vectors have been omitted for clarity. Only induction vectors with lengths >0.15 are depicted because the directions of smaller vectors are undetermined within their statistical confidence intervals. The induction vectors indicate geoelectric strike directions between N30° W and N60° W.

using the entire period range. The strike estimates range between N 30° W and N 60° W (with a 90° ambiguity). Since all periods were used for the estimation of the strike directions, they include the intermediate period range with moderate 3-D effects. A multiperiod multisite optimization of all sites and periods simultaneously yields a strike direction of N 42.5° W, which is indicated by the solid black lines in Fig. 6(a). We also determined strike directions for different period ranges of one decade each. These decade-wide multisite strike estimates (not shown) compare well with the single-site and multisite estimates of Fig. 6(a). The rose diagram in Fig. 6(b) summarizes the directions of the real induction vectors. The orientation of the induction vectors is generally in good agreement with the impedance strike estimates, which both indicate a geoelectric strike direction in the range N 30° W and N 60° W; the overall best-fitting estimate is N 42.5° W.

The ellipticities ϵ_x and ϵ_y of the impedance tensor columns rotated to N 42.5° W are depicted in Fig. 7 in terms of pseudo-sections for all sites and periods. White colours correspond to vanishing ellipticities; grey to black colours indicate increasing absolute ellipticties and hence stronger 3-D effects. Lines indicate the available data at each site. For our data set, 3-D effects are evident in the second column of the impedance tensor (Z_{xy}, Z_{yy}) and at periods >1000 s. Moderate 3-D effects occur at profile distances between −10 and 0 km in the period range ∼10–100 s and at profile distances >10 km. However, the majority of the data appear to be 2-D and in agreement with a strike direction aligned with the SAF.

It is noteworthy that observed 3-D effects are almost exclusively identified with the second column of the impedance tensor, that is, associated with the presumed E-polarization impedance. This is in accordance with Wannamaker (1999) who suggested that the E-polarization impedance is more susceptible to 3-D effects than the H-polarization impedance. However, we found that for our data set the H-polarization impedance adds little information to the deep structure. This response appears to be controlled mostly by upper crustal heterogeneities, similar to the effects described in Becken *et al.* (2008).

2.3 Downweighting of 3-D effects

There is no mathematically rigorous concept for treating data with 3-D effects in the scope of a 2-D inversion. One approach is to downweight the influence of 3-D data by increasing the error bars proportional (in some way) to the deviation from a 2-D response. Booker *et al.* (2005) increased the impedance error bars until a distortion model fitted the data with an acceptable misfit. However, they considered the misfit over all periods at a particular site and obtained the same error floor at all periods.

Here, we use the ellipticities ϵ_x and ϵ_y to quantify the deviation of the data from the desired 2-D response at each period. Vanishing ellipticities are consistent with 2-D conditions and non-vanishing values are indicative of 3-D effects. Therefore, we increase the error bars of the impedance elements systematically at each period until the corresponding ellipticities vanish within their confidence limits. Effectively, the impedance error bars are increased until a 2-D response cannot be distinguished from a 3-D response within the new confidence limits of the data.

Since it is impossible to directly back-project ellipticity confidence intervals onto the impedance errors (two ellipticities are derived from four impedances), we assume equal errors within each row of the impedance tensor, similar to Booker *et al.* (2005). This implies that impedance errors are only due to noisy electric field components, which is in accordance with the usual assumptions

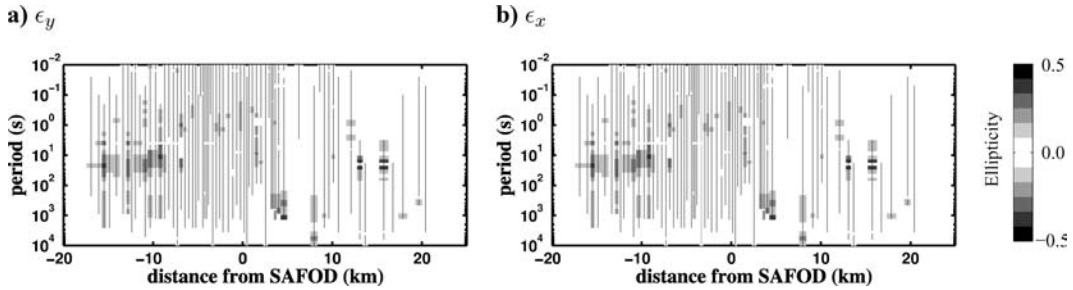

Figure 7. Pseudo-sections of ellipticities of the impedance tensor rotated to the multisite multiperiod strike estimate of N42.5°W. (a) Ellipticities ϵ_y derived from the impedance elements (Z_{xx}, Z_{yx}) and (b) ellipticities ϵ_x derived from (Z_{xy}, Z_{yy}). Lines indicate available data used for the analysis. White and light grey colours correspond to small ellipticties and indicate 2-D conditions; dark grey and black colours indicate 3-D conditions.

for the least-squares approach in MT data processing. Under this assumption, the errors of the two ellipticities become coupled and allow a unique back-projection onto the impedance errors. This procedure is illustrated in Fig. 8 using the rotated impedances of site 20 (*cf.* Fig. 2). Fig. 8(a) shows the impedance elements with modified error bars, yielding up to 8° error bars for the phases at intermediate period ranges; associated ellipticties with corresponding confidence estimates are depicted in the upper panel of Fig. 8(b). Note that, as a result of the modified impedance errors, the error bars of the distortion angles (lower panel of Fig. 8b) also become larger when compared with the original estimates (*cf.* Fig. 2).

We use a similar approach to modify error bars of the vertical magnetic transfer functions. In order to downweight period ranges with non-vanishing components of T_x a larger error bar is imposed on the respective values of T_y. We use the absolute values of T_x as a measure of the deviation from the 2-D response and apply the same error bars to the real and imaginary parts of T_y.

3 RESISTIVITY MODEL

3.1 Inversion strategy

In the case of a 2-D Earth, the inverse problem of finding a 2-D electrical resistivity [$\rho(y, z)$] model that can explain the observed data reduces to fitting the two E- and H-polarization impedances (Z_{xy} and Z_{yx} in the $-59°$ rotated coordinate system, respectively) and one element of the geomagnetic transfer functions (T_y in rotated coordinates). We used the data of the 66 sites from the profile (see Fig. 1) in the period range $T = 0.01$–$10\,000$ s and employed the inversion scheme of Rodi & Mackie (2001).

The subsurface electrical resistivity distribution is represented on a grid consisting of 242 × 72 rectangular cells in the *y*-and *z*-directions, respectively, with constant resistivity in each cell. Electric and magnetic fields are computed on the same grid using a finite-difference scheme (Madden 1972; Mackie *et al.* 1988). The modelled domain is much larger than the actual region of interest to ensure that the model boundaries are sufficiently far away from resistivity anomalies in order to satisfy the boundary conditions. Here, the modelled domain spans 1000 × 340 km in the *y*- and *z*-directions, respectively. The smallest cells used are 150 × 30 m, approximately 1/2 × 1/10 of the skin-depth $\delta_s = 503\sqrt{\rho T} \simeq 350$ m at the shortest period $T = 0.01$ s used in this study and assuming an average resistivity of $\rho = 50\ \Omega$ m; these cells are located at the surface just below the sites. Clearly, the cell sizes can be increased progressively with increasing depth and distance from the profile, because deep and/or remote structure is only sensed by long-period fields with correspondingly large skin-depths. We determined geometrical spreading factors by trial and error to achieve a good compromise between the total model dimension and the total number of cells, while ensuring that cells are kept sufficiently fine for accurate numerical calculations.

For the inversion, we employed the minimum structure, non-linear conjugate gradient 2-D inversion of Rodi & Mackie (2001). This program minimizes a Tikhonov regularized functional $\Phi = \chi^2 + \tau\mathbf{L}(\log\rho)$ as a trade-off between a structure penalty functional $\tau\mathbf{L}(\log\rho)$ and the data residual norm weighted with the data variances (χ^2). $\mathbf{L}$ is a weighted integral of the Laplacian squared of the model. Weighting increases both horizontal and vertical derivatives by a factor equal to the size of the each model element. This structure penalty generates increasingly smooth structure with increasing depth and distance from the profile (due to increasing cell sizes).

As mentioned in Section 2.2, static shift cannot be removed from the data prior to modelling. In order to avoid artefacts resulting from static shift in the data, we put more emphasis on fitting the static-shift-free impedance phases and induction vectors; apparent resistivities are downweighted using enlarged error floors. Recall, that static shift originates from charge accumulations at small-scale 3-D heterogeneities. 2-D modelling can, at least to some extent, reproduce the effect of charges in the H-polarization by placing small-scale anomalies near the surface. However, static-shift in the E-polarization cannot be simulated in a 2-D modelling assumption, and as a consequence, E-polarization apparent resistivities should not be given too much weight in the inversion. Therefore, we downweight the influence of the E-polarization apparent resistivities on the inversion by assigning an error floor of 100 per cent. The H-polarization apparent resistivities are downweighted using an error floor of 10 per cent, because static shift can to some extent be reproduced by the inversion model. The impedance phases and induction vectors are free of static shift and are given relatively higher weights (1° and 0.03 error floors, respectively) for the inversion. These values represent the results of trial and error tests and yielded a good fit of the phases and induction vectors while at the same time reproducing the shape of apparent resistivity curves. However, as explained in Section 2.3, phase data and induction vectors in period ranges where 3-D effects are visible, are downweighted by increasing their error bars to be consistent with the 2-D assumption.

3.2 Starting models and inversion models

MT data are sensitive to conductors beyond the profile. We therefore, include the Pacific Ocean *a priori* in the starting model using a simplified bathymetry and average sea-water resistivity of 0.3 Ωm. The resistivity of the ocean was fixed for inversion; however, the inversion was allowed to generate a smooth transition from the ocean

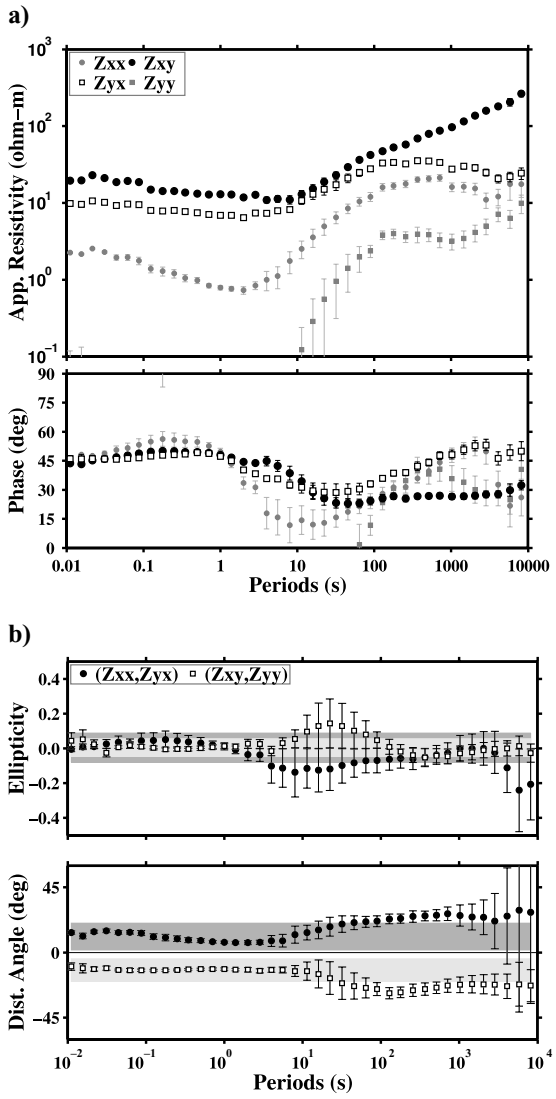

Figure 8. Treatment of 3-D effects (with non-vanishing ellipticities). (a) Apparent resistivities and phases with modified error bars consistent with 2-D conditions. (b) The ellipticities are used to measure the deviation of the impedance data from the desired 2-D response. Ellipticities are shown with modified confidence limits consistent with a 2-D assumption. Associated error bars of distortion angles have been implicitly modified.

into the underlying subsurface as this could represent ocean-water saturated sediments at the seafloor.

Preliminary inversions, based upon a starting model incorporating the Pacific ocean within a homogeneous half-space (50 Ωm) resulted in unrealistically high conductance (vertically integrated conductivity) >15 000 S for the Earth's crust between the SW end of the profile and the coast. Effectively, the inversion replaced the effect of the ocean with a nearby bulky conductor. For the structure below the profile (for which we have data coverage) this can result in a bias due to coupling of currents between spurious off-profile features and conductors beneath the profile.

The inclusion of a more resistive crust represents much better the inland decay of the electromagnetic fields associated with excess currents at the oceanic shelf. Trial and error forward modelling revealed that a resistive crust (1000 Ωm) between the shelf and the measured profile and embedded in a homogeneous 50 Ωm background model helps to explain the observed induction vectors at periods >1000 s. A resistive crust is also in accordance with the results of large scale, lower resolution studies near Parkfield (Park & Biasi 1991) and Hollister (Mackie *et al.* 1988). The thickness of resistive crust in the starting model could extend into the lithospheric mantle (which is assigned the background resistivity of 50 Ωm in the starting model) but we limited the thickness to 30 km for the starting model, which is in principal structural agreement with the geological cross-sections of the Coast Ranges presented in Zoback (2002).

The lateral extent of resistive crust in the starting model influences the outcome of the inversion. Using a resistive layer in the starting model, which extends along the entire model, results in an inversion model with unacceptably high normalized root mean square misfit (nrms = 5.9): the inversion was trapped in a local minimum. To find a model better fitting the data, the resistive layer had to be terminated or interrupted beneath the profile. In Fig. 9(a), we show the inversion models obtained for three different starting models: in model 1 (left-hand panel), the resistive layer (1000 Ωm, hatched area) was terminated at the SAF; model 2 (middle panel) was calculated from a starting model with the resistive layer being terminated at the SW end of the profile; model 3 (right-hand panel) combines resistive crust to the SW and the NE of the SAF, which is interrupted by a 10 km wide moderately conductive zone (50 Ωm) near the SAF. The extent of resistive crust in the starting model is indicated by the hatched area (*cf.* Fig. 9a); the remaining area of the starting model consists of a 50 Ωm half-space and a 0.3 Ωm Pacific ocean. Note that the models in Fig. 9 show a larger section than that for which we have profile coverage. In our final interpretation, we will concentrate on the profile part of the cross-section, but at this stage it is important to consider the effect of features beyond the extent of the profile.

The major conductive and resistive features [C1–C2 and lower crustal zone (LCZ), red colours and R1–R3, blue colours] of the inversion models 1–3 obtained from the three starting models are similar and the achieved data fit is almost indistinguishable (nrms = 1.50–1.51). C1 is a broad conductive zone within the upper mantle at depths >30–40 km. This conductor is clearly confined to the Pacific plate and terminates ∼10–15 km to the SW of the SAF. C1 underlies a massive resistive crustal block (R1), which extends from ∼5–25 km depth and terminates ∼10–15 km to the SW of the SAF (similar to the mantle conductor C1). The lateral extent of C1 and R1 is independent of the extent of resistive crust in the starting model. A separate upper crustal resistor (R2) appears adjacent to R1. R2 extends from ∼1 to 8 km depth, is clearly disconnected from R1 to the SW and terminates near the seismogenic zone of the SAF to the NE. Farther to the NE, that is, across the SAF, a prominent crustal conductor (C2) is imaged. C2 reaches from near-surface to more than 10 km depth; it is laterally sandwiched between R1 to the SW and a further prominent, isolated resistor (R3) to the NE. In addition to these major structures, all inversion models show near-surface conductive layers towards both profile ends and a number of small-scale conductive features in the vicinity of the SAF.

All three inversion models in Fig. 9(a) indicate the existence of conductive lower crust beneath the SAF (labelled LCZ, lower crustal conductive zone). However, this region exhibits some dependency on the starting model. In model 1 (left-hand panel), where the resistive crust in the starting model was extended to the SAF, resistivities of <10 Ωm (yellow colours) within the lower crust are confined to the NE of the SAF. In this inversion model, the upper crustal conductor C2 appears subvertical and extends into the lower crust. Inversion model 2 (middle panel) suggests a SW-dipping conductor C2 with

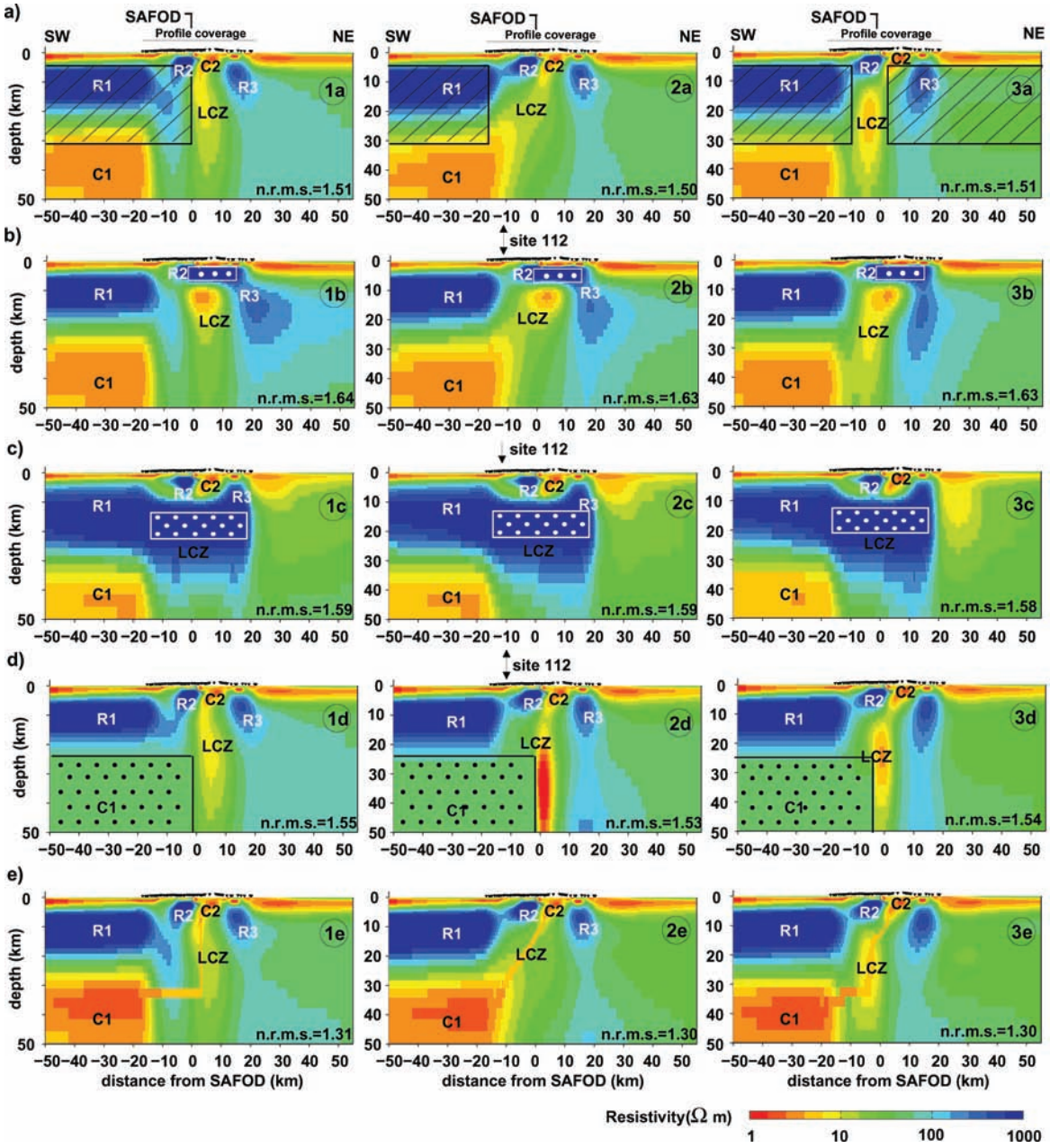

Figure 9. Model appraisal I: (a) Inversion models obtained for three different starting models (models are labelled 1–3 from left to right). The starting model consists of a resistive crust (1000 Ωm) indicated by the hatched area, which is embedded in a homogeneous half-space (50 Ωm). The ocean is included in all starting models. Enumerated labels R and C denote prominent resistors and conductors; LCZ lower crustal conductive zone. Model tests in (b)–(d) use modifications of these models as the starting model. (b) Constrained inversion result with a subregion of the upper crustal conductor C2 constrained to be resistive (the region outlined with the white rectangle was constrained to 1000 Ωm). (c) Constrained inversion results with the LCZ constrained to 1000 Ωm (white rectangle). (d) Constrained inversion results with the conductor in the upper mantle (C1) constrained to 50 Ωm (black rectangle). (e) Inversion models with C2, LCZ and C1 interconnected *a priori* yield a significantly improved data fit. In this case, the smoothest deviation from the starting model was sought. The achieved nrms is given for all models. Phase responses for the models 2a–2d are shown in Fig. 10 for a number of sites. In summary, model variations 1a–3a and 1e–3e are consistent with the data; the rest of the models are rejected.

a connection to mantle conductor C1 at lower crustal depths and hence across the SAF. Inversion model 3, which was obtained from a starting model combining resistive crust to the SW and the NE of the SAF, yields a high-conductivity body at lower crustal depths which is separated from C2 and C1 by narrow zones with moderate resistivity (10–30 Ωm).

As mentioned previously, the achieved nrms obtained for these three models is very similar. A more detailed inspection of the model responses revealed that the modelled MT responses for the three different models in Fig. 9(a) are indeed similar at all sites and periods (e.g. the impedance phases are similar to within ∼2°). Hence, there is no significant difference in the nrms value as a global measure nor can we observe systematic, significant difference in the fitting of local data subsets with either of the models. Hence, the small differences in the model responses of models 1–3 are not sufficiently significant to give preference to a particular model. All three inversion

models suggest a lower crust below the SAF containing anomalously high conductance; however, the geometrical distribution of zones with low resistivity (<10 Ωm) and moderate resistivities (~10–30 Ωm) can not be uniquely resolved from the MT data.

In the following section we discuss these major features of the resistivity models and evaluate their robustness using constrained inversion.

3.3 Constrained inversion models

In Figs 9(b)–(d) we show inversion results using variations of the models 1–3 in Fig. 9(a) as starting models with the variations constrained throughout the inversion, and compare associated model responses for selected representative sites (Fig. 10) and data residuals with those of the unperturbed model. For clarity, we concentrate on model responses in terms of impedance phases and on the variations of model 2 (middle panels in Fig. 9). These tests allow us to evaluate alternative models and determine if they are inconsistent with the data or if the models contain spurious features required to fit the data (e.g. extreme resistivity values or unrealistic conductances).

With a first test the significance of the upper crustal conductor C2 was examined. For the inversion, a rectangular region between resistors R1 and R3 was constrained to 1000 Ωm in the depth range 2–6 km (outlined with a white rectangle and dots in Fig. 9b). These models (1b–3b) achieve an overall nrms misfit of 1.62–1.64 but

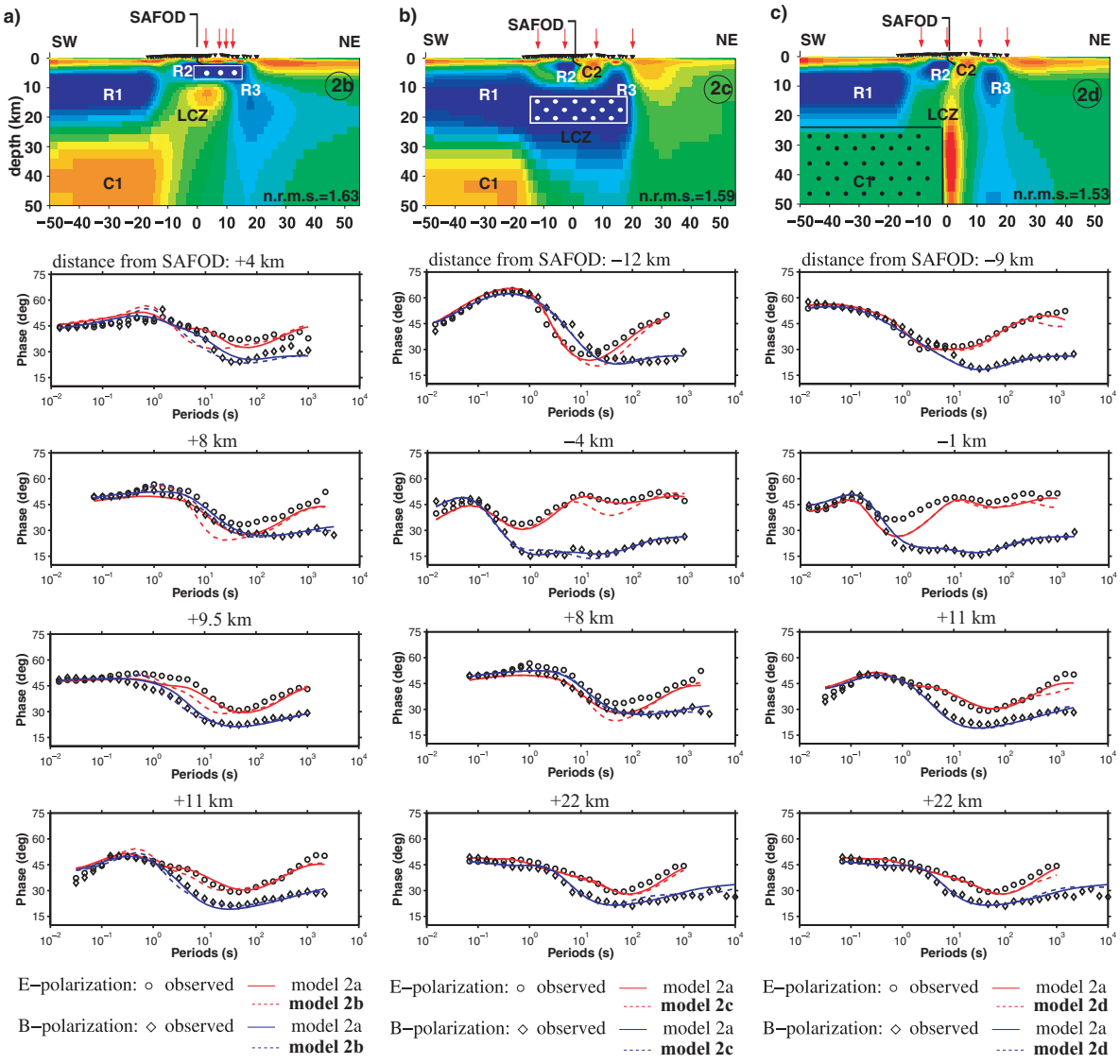

Figure 10. Model appraisal II. Data fit for the constrained inversion models in the middle panels of Fig. 9. Top panels show the model variations 2b–2d (from left- to right-hand side), lower panels show corresponding modelled impedance phases (dashed lines) in comparison to the observed data (open symbols) and to the phases modelled for model 2a (solid lines; *cf.* Fig. 9a, middle panel, for model 2a). For each model variation, we compare modelled and observed phases for four representative sites; the site locations are indicated with red arrows in the upper panels and profile distances (distance from SAFOD) are given on top of each phase plot. (a) Model variation 2b generates impedance phases fitting the observations significantly worse (period range 1–100 s) than the phases modelled for model 2a. In particular, the E-polarization phases for the model variation 2b are too low suggesting that a resistive connection between resistors R2 and R3 disagree with the observations. (b) Phases modelled for the model variation 2c are systematically too low in the period range 10–300 s suggesting that the existence of a resistive lower crust connecting resistors R1 and R3 across the SAF can be refuted. (c) Constraining the region of the mantle conductor C2 to moderate resistivities (50 Ωm) results in a degraded fit of the E-polarization phases at periods longer than ~500 s. Only a few periods are affected by this model variation, hence the overall nrms is only slightly degraded.

the misfit at sites located above the constrained region is increased by up to 0.5 which is significantly worse when compared to the responses of the original models (Fig. 9a; nrms = 1.50–1.51). The impedance phase responses for the model variation 2b (middle panel in Fig. 9b and upper panel in Fig. 10a) are depicted in the lower panels of Fig. 10(a) in comparison to the phase responses of model 2a and to the observed data. We show these responses for four sites located above the constrained region at profile distances 4, 8, 9.5 and 11 km (NE of the SAFOD). The site locations are marked with red arrows above the model in Fig. 10(a). From the phase plots it becomes obvious that the model variation 2b generates systematically lower E-polarization phases (dashed red lines) in the period range ∼1–100 s when compared to the original model response (solid red line) and to the observed data (open circles). A similar but less pronounced effect can be observed for the H-polarization phases (blue lines and open diamonds). Hence, constraining the region between the R2 and R3 as resistive is incompatible with the observations.

Note further that the constrained inversion models in Fig. 9(b) exhibit extremely low resistivities (0.3 Ωm) just above the constrained zone and the LCZ appears as a distinct conductive body which is pushed upwards when compared with the original models. This suggests that the inversion attempted to re-establish a continuous conductive zone between shallow depths and deep crust.

The inversion models in Fig. 9(c) were constrained to contain a resistivity of 1000 Ωm in the depth range 15–25 km between profile distance −15 and +20 km (outlined with a white rectangle) in order to confirm the existence of the LCZ. The model variations 1–3c achieve an overall nrms misfit of 1.58–1.59, worse than that of the original model (Fig. 9a; nrms = 1.50–1.51). In further inversion tests (not shown), we additionally fixed the model during the inversion outside of a rectangular region, extending from −50 to +60 km profile distance and from the surface to a depth of 50 km, that is, we also constrained the deeper parts and the off-profile regions of the model to the starting model. In this case, the data fit was worse (nrms > 1.65). This means that some of the off-profile features can partly reproduce the effect of the LCZ. However, the effect of the originally contained conductance of the LCZ within the lower crust can not be fully compensated for with off-profile features, as the data fit is in both inversion tests (i.e. with and without the deeper and off-profile parts of the model held fixed) degraded when compared with the unconstrained inversion.

In Fig. 10(b), we compare the phase responses for the model variation 2c with the responses of the original model 2a and the observed data. The model with the lower crust constrained to 1000 Ωm produces E-polarization phases in the period range ∼10–300 s that are systematically too low (*cf.* lower panels in Fig. 10b). This effect can be observed along the entire profile (see red arrows above the resistivity model in the upper panel of Fig. 10b for site locations). In turn, the H-polarization impedance phase is less affected by the presence of a resistive lower crust.

With a lower crust constrained to a resistivity of 1000 Ωm, the inversion attempts to enlarge the upper crustal conductor (C2), pushing it at the same time to greater depths in order to achieve a higher conductance in the lower crust, similar to the unconstrained model. Additionally, the high-conductivity layer near-surface to the NE of the profile (original model) is pushed to depths greater than 10 km. Regardless, this does not result in a model which fits the observed data equivalently well. In summary, the MT data require high conductivities at lower crustal levels in the central part of the profile; a continuous high-resistivity lower crust is not in agreement with the observations.

Finally, we tested the region containing the mantle conductor C1 by constraining the resistivity in this area to 50 Ωm, similar to the resistivity of the surrounding mantle. Inversion models obtained for this model variation are depicted in Fig. 9(d); the constrained region is indicated by a dotted black box in models 1d–3d. The achieved overall nrms data fit (1.53–1.55) is slightly worse when compared with the original models in Fig. 9(a). Similar to the discussion above, the conductance originally contained in the model is partly compensated for by adding conductance to the model off the profile. In this case, the conductivity of the subsurface below the ocean is significantly increased.

Phases responses of this model variation are shown in Fig. 10(c) in comparison with those of the original model and the observed data. While the H-polarization phases are virtually unaffected by the removal of the uppermantle conductor C1, the E-polarization phases for model variation 2d are too low at periods $\gtrsim$500 s. Despite the fact that the nrms values for the original model and the model variation indicate—as a global measure of data residuals—a similar degree of overall data fit (with a change in nrms of ∼0.03), inspection of the individual sounding curves suggests that the absence of the mantle conductor C1 causes systematically degraded data fit of the long-period E-polarization phases. These modelling results suggest also that only the E-polarization data exhibit sensitivity to upper-mantle conductivity with the H-polarization appearing indifferent to variations of the model at upper-mantle depths.

3.4 *A priori* inversion models

Models 2 and 3 in Fig. 9(a) imply a conductive connection between the mantle conductor C1 and the upper crustal conductor C2 across the lower crust (LCZ). In further variations of the models in Fig. 9(a), we introduced a connection between the upper crustal conductor C2 via the LCZ to the upper-mantle conductor C1 by a ∼5 km narrow conductive zone of 4 Ωm. We used this model as an *a priori* model for subsequent inversions. For the inversion, the resistivity structure of an *a priori* model, ρ_0, is incorporated in the structure penalty term as $\tau\mathbf{L}(\log\rho - \log\rho_0)$, that is, the inversion seeks a trade-off between data residuals and deviations of the inversion model from the *a priori* model. For simplicity, we use the same regularization parameter τ and penalty function $\mathbf{L}$ as in the previous inversions based on regularized model smoothing.

The inversion models using this *a priori* inversion strategy are depicted in Fig. 9(e). Model 1 (left-hand panel) was modified to contain an *a priori* conductive channel, which runs horizontally at a depth of ∼30 km and then connects vertically to C2 through the LCZ. In model 2, we directly connected C1 and C2 with a 45° dipping conductive channel; for model 3 we connected C1 with the high-conductivity body within the LCZ by a subhorizontal conductive channel, which continuous subvertically into the upper crust and into conductor C2.

The overall misfit for these models is nrms = 1.30–1.31, and data residuals improved at most sites. Clearly, all of these models achieve a dramatically better data fit than the models shown in Fig. 9(a). In all three models, the *a priori* conductive channel is maintained by the inversion procedure. Together with the improved data fit, this suggests that the *a priori* inversion models (Fig. 9e) are not only consistent with the data, but that they may even be a better representation of the data than the models in Fig. 9(a).

The amount of conductance added to the models by the inclusion of a conductive channel is not very large. The improvement of the

data fit is at least partly caused by allowing current flow from the upper mantle into the upper crust. Effectively, the *a priori* channel adds a short-circuit between C1, LCZ and C2 to the model in Fig. 9. The exact geometry of this short-circuit appears to play a minor role in its effect on the responses at the surface. However, the structure penalty term employed in the *a priori* inversion does allow for changes elsewhere in the model, in particular in regions where a minor adjustment of the *a priori* model can improve the data fit. Hence, improved data fit is also a consequence of the modified structure penalty, leading to a different trade-off between structure penalty term and data residuals, that is, effectively to a different class of inversion models.

Why does the inversion not find the short-circuit between C1, LCZ and C2 automatically? In the original inversion models both the lower part of C2 and the LCZ are sandwiched between resistors (see Fig. 9a). A sharp resistivity contrast of a high-conductivity zone enclosed by resistive regions will be reproduced in a smoothing regularized inversion by a model with less prominent high conductivity spread over a broad area (to maintain conductance). Recall that the inversion models shown in Figs 9(a) and (e) were obtained as a trade-off with the different structure penalty terms $\tau\mathbf{L}(\log\rho)$ and $\tau\mathbf{L}(\log\rho - \log\rho_0)$, respectively. The first inversion strategy seeks smoothness while the latter seeks to maintain features of the *a priori* model. To quantify model roughness with the same measure, we recomputed the structure penalty term $\tau\mathbf{L}(\log\rho)$ for the *a priori* inversion model in row e of Fig. 9 instead of the term $\tau\mathbf{L}(\log\rho - \log\rho_0)$ used in the inversion. These values are significantly larger than for the other models in Fig. 9. For instance, the values of the structure penalty term for the models with and without a narrow channel of high conductivity (models 2e and 2a, respectively, in Fig. 9) are 152 170 and 9780, that is, the narrow conductive region impacts the model structure penalty term by a factor of 15. On the other hand, the data residuals (χ^2) are improved from 22 073 to 14 785, corresponding to a factor of 1.6. This explains, why the smooth inversion procedure does not favour a narrow conductive region for the LCZ and why the *a priori* inversion with a narrow conductive zone can achieve such a significantly improved data fit.

We cannot objectively decide if the inversion models in Fig. 9(e) are to be preferred over the models in row a of Fig. 9 or not, because these models belong to different model classes with different trade-off functionals, which means that a direct comparison of nrms values is not necessarily meaningful. However, we can conclude that a narrow conductive zone reaching from the upper mantle to the upper crust as in the models in Fig. 9(e) is not in contradiction with the measured MT data.

3.5 Final resistivity model and data fit

Having tested important large-scale features of the resistivity models and the dependency on the starting models, we concentrate now on the crustal part of model 2a and on the section for which we have profile coverage. Among the three model types 1–3 discussed in the previous sections, model 2 exhibits least structure within the LCZ and represents, therefore, a best trade-off in a sense of the smooth inversion model space. Furthermore, models 1 and 3 appear to be biased by the particular choice of starting model, since the LCZ in the inversion model exhibits some spatial similarity in the termini of resistive crust within the respective starting model. For these reasons, we concentrate in the sequel on model 2a, keeping in mind that models 1a and 3a with a similar data fit agree with our interpretation. Although model 2e (as well as models 1e and 3e) achieved the best data fit, we prefer to base our interpretation on the minimum structure inversion model 2a that was obtained without *a priori* information.

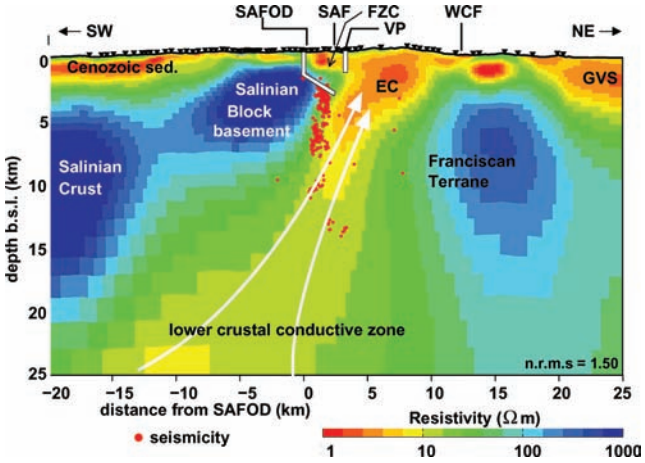

Figure 11. MT resistivity model along the 45 km profile across the SAF near the SAFOD site. Superimposed on the models are the SAFOD main hole and the Varian–Philips (VP) well; red dots indicate the seismicity (Thurber *et al.* 2006) within 3 km distance from the profile. We speculate that a deep-reaching subvertical corridor of high conductivity, linking the upper crustal eastern conductor (EC) with a lower crustal conductivity zone (LCZ) and further with a mantle conductor, images a channel for deep crustal or mantle fluids (sketched with white arrows). This channel is enclosed by the resistive Salinian Block basement and Salinian Crust to the SW and a resistive block in the NE at mid-crustal levels (labelled Franciscan Terrane). At the SW end of the profile, above the resistive Salinian Crust, the model indicates a 2 km thick conductive layer near-surface, that coincides with low seismic *P*-wave velocities (1.5–3.5 km s^{-1}) (Hole *et al.* 2006) and can be attributed to presumably Pliocene and Miocene marine sediments (Diblee 1972). The model recovers also the shallow fault-zone conductor (FZC) below Middle Mountain (e.g. Unsworth *et al.* 1997). The sediments of the Great Valley Sequence (GVS) could be responsible for the high conductivity imaged in the upper crust of the NE part of the profile.

The responses predicted from model 2a (Fig. 9a, middle panel) are depicted in the right-hand panels of Fig. 3 in comparison with the measured data (left-hand panels in Fig. 3). The model yields good data fits at all sites and periods; only the modelled E-polarization phase responses between profile distances 0 and −10 km at periods longer than ∼10–100 s yield lower values than observed. This implies that the deep structure, that is, lower crust and/or upper mantle would be even more conductive than shown in our model (Fig. 11). However, as this region also exhibits some 3-D effects (*cf.* Fig. 7), the corresponding data were downweighted for the inversion. The increased misfit of this data subset with 3-D effects is, therefore, expected.

Our preferred model for the interpretation is shown in Fig. 11. The most prominent conductor imaged in this model is the eastern conductor (EC, corresponding to C2 in Fig. 9) between the SAF and the Waltham Canyon fault (WCF), which widens into the LCZ. Unsworth & Bedrosian (2004) speculated that the EC may represent a zone of overpressured crustal fluids, which may have pathways into the SAF. In contrast to our resistivity model, the model of Unsworth & Bedrosian (2004) gave the impression that the EC may represent a synclinal structure with a clearly defined bottom. With the longer profile of this study, we are able to better resolve deeper structure and hence that the SW-ward dipping geometry of the EC reaches depths of more than 10 km.

Additional high-conductivity zones include the fault zone conductor (FZC) of the SAF (Unsworth *et al.* 1997, 1999, 2000;

Unsworth & Bedrosian 2004) associated with the damage zone of the SAF (Ritter *et al.* 2005), a near-surface conductive layer in the SW part of the profile presumably related to Cenozoic marine sediments and a NE-ward dipping conductive zone in the NW part of the profile, which can be associated with the sediments of the Great Valley Sequence (GVS) (Diblee 1972). Another isolated conductivity anomaly has been imaged NE adjacent to the WCF. This feature may be related to a synclinal structure indicated in the geological map (Diblee 1972), which may bear sediments of the GVS.

Consistent with the general geological setting, the resistors located to the SW of SAF are attributed to the Salinian formation; resistors within the northeastern fault block are considered as part of the Franciscan formation (labelled Franciscan Terrane). Hence, the resistive blocks R1 and R2 (*cf.* Fig. 9) are denoted as Salinian Crust and Salinian Block basement. R3 could represent a competent sliver of oceanic crust within the Franciscan formation.

3.6 Comparison with other geophysical data

The upper part of the crustal block of the granitic Salinian Block basement was drilled by the SAFOD. The lateral extent of the resistor from −9 to +1 km distance from the SAFOD correlates spatially with a static magnetic field anomaly (McPhee *et al.* 2004), suggesting that this granite is magnetic. Airborne magnetic data are in agreement with our model in suggesting that this anomaly is different from the adjacent non-magnetic basement (Salinian Crust) farther to the SW. A body with a similar magnetic signature was found on the North American side of the SAF in the Mojave Desert, 300 km to the SE (Roberts & Jachens 1999; McPhee *et al.* 2004); an offset that may represent the entire slip along the SAF.

The separation of the Salinian Block Basement from the Salinian Crust to the SW and at greater depths correlates with a subvertical zone of high seismic reflectivity (Buske *et al.* 2006), which is imaged at ∼ −15 km profile distance in the depth range ∼5–15 km. We speculate that both observations are expression of a deep-reaching fault zone, separating between R1 and LCZ. Near-surface, the assumed fault coincides approximately with the NE-ward thinning of Cenozoic sediments at −10 km profile distance. This could indicate that the fault was active as a post-sedimentary thrust in Cenozoic times.

The bottom of the resistive Salinian block basement is spatially related to a seismic reflector band at ∼8 km depth (Bleibinhaus *et al.* 2007). A second horizontal reflector was imaged at ∼12 km depth. We tested therefore, if the resistive block could extend to greater depths. These tests (not shown) confirm that our data are consistent with a resistive Salinian block basement extending to the bottom of the seismogenic zone (∼12–15 km depth). However, such a deep-reaching block would complicate explanations of the shallow horizontal reflector at a depth of ∼8 km, as it would be located within the Salinian block basement.

To the NE of the SAF, the seismic reflection profile (Hole *et al.* 2006; Ryberg *et al.* 2005; Bleibinhaus *et al.* 2007) images the WCF as a NE-ward bended listric fault in the depth range 2–4 km. This listric reflector is slightly offset to the SW of the surface exposure of the WCF but correlates spatially with the NE terminus of the EC in this depth range. The WCF appears to be associated with a fault zone conductor in the shallow crust, similar to the FZC of the SAF. The WCF, however, is a thrust fault, where steeply upturned marine sediments of the Great Valley Sequence (GVS) are intensively faulted and folded (Diblee 1972). Carena (2006) used relocated earthquakes from the years 1980–2006 and identified an active reverse fault E of the SAF that abuts the SAF near the bottom of the seismogenic crust at ∼15 km and reaches near-surface close to the WCF. This fault correlates with the lower SW-dipping bound of the EC and suggests that this boundary is fault-related. Carena (2006) attributes the formation of the Parkfield Grade mountain range, which has the highest relief in the region, to the presence of this SW-dipping fault, an interpretation that could provide deep-reaching thrust-fault-related fractures and interconnected porosity on a large scale.

Further to the NE, the NE-dipping top of resistor R3 could be related to the thrust/backthrust system discussed by Guzofski *et al.* (2007), which was responsible for the 1983 Coalinga earthquake. The top of R3 coincides with high seismic *P*-velocity data (Thurber *et al.* 2006) and re-interpreted reflection data (Guzofski *et al.* 2007) near Coalinga, which image a NE dipping high-velocity body at >10 km depth.

The crustal 3-D seismic velocity model of Thurber *et al.* (2006) indicates a zone of anomalously low *P* velocities (<5.5 km s^{-1}) NE of the SAF down to depths of ∼15–20 km, which coincides with the electrically conductive middle to lower crust. Resolution of the seismic velocity structure is limited to ∼15–20 km depth and can, therefore, not be used to construct additional constraints for the LCZ at greater depths.

4 A DEEP CRUSTAL FLUID CHANNEL INTO THE SAF

The most intriguing feature of the regional electrical resistivity model in Fig. 11 is the approximately 5–8 km wide, subvertical corridor of high electrical conductivity connecting the upper crust (EC in Fig. 11) with the lower crust. This zone of high conductivity reaches the near-surface 5–10 km NE of the SAF. Resistivities of less than 5 Ωm are found within the EC to a depth of 8–10 km adjacent to the SAF. From there, the anomaly appears to link with the lower crustal conductive zone (LCZ) at non-seismogenic depths (>12–15 km). Constrained inversions of the model in Fig. 11 revealed that removal of the upper branch of the high-conductivity zone (EC) or its LCZ significantly increases data misfit (Figs 9b and c). Vice versa we can significantly improve data fit, if the conductive mantle and the LCZ are *a priori* connected with the EC by a ∼5 km wide conductive (∼5 Ωm) channel (Fig. 9e). We discussed in Section 3.4 that resistivities between 10 and 30 Ωm in the depth range >12–15 km, as indicated by the minimum structure inversion model in Fig. 11, represent an optimal trade-off between data misfit and model regularization.

We speculate that this deep-reaching conductivity anomaly is caused by fluids. For high electrical conductivity, ionic conduction (the dominant conduction mechanism in fluid-saturated rock) requires open pores or fractures which are interconnected over significantly large distances (kilometre range). Consequently, this zone of high conductivity may represent a possible pathway for crustal fluids. If this high-conductivity zone reflects a fluid channel, its upper branch (EC) is offset to the NE from the currently active SAF.

Fig. 12 represents a collage of the crustal section in model 2e (*cf.* Fig. 9e), an annotated zoom-in of the same model near the SAFOD and the results of geochemical analyses of noble gases (Wiersberg & Erzinger 2007; Kennedy *et al.* 1997). When considering high conductivities as a proxy for increased volumes of interconnected fluids, possibly associated with a changing pore geometry to a predominantly crack-like arrangement, both the borehole measurements and the resistivity model yield a consistent picture. Measurements in the SAFOD main hole yield a fluid pressure contrast across the fault

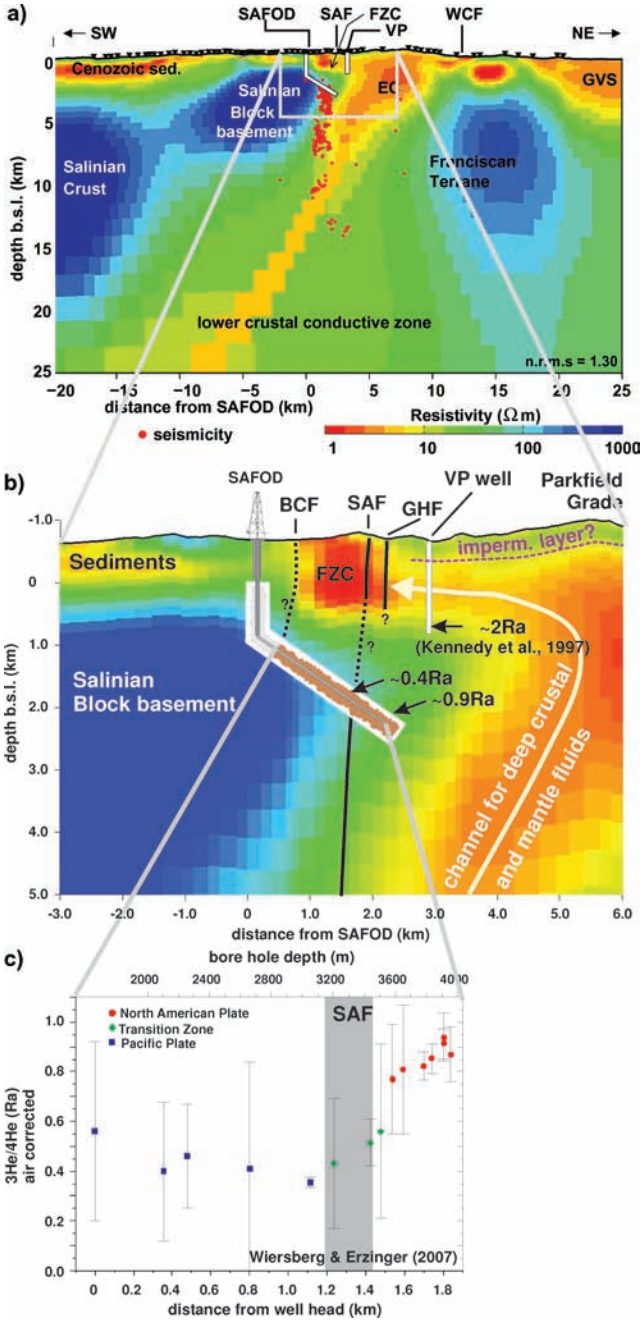

Figure 12. Relation between the resistivity model and measured ^{3}He/^{4}He ratios. (a) Crustal section of the inversion model with an *a priori* conductive channel (*cf.* Fig. 9). (b) Zoom into the resistivity model near the SAFOD. (c) ^{3}He/^{4}He ratios from mud-gas logging at the SAFOD. The upper branch of the crustal high-conductivity zone is offset to the NE from the SAF. Increasing ^{3}He/^{4}He ratios on the North American Plate, observed both within the SAFOD and the Varian–Phillips (VP) well indicate increased mantle derived fluid content. Furthermore, elevated pore pressure to the NE of the SAF (Zoback *et al.* 2006) and overpressured fluids reported from the nearby VP well 1.4 km NE of the SAF (Johnson & McEvilly 1995) suggest a fluid trap within the NE fault block. From these observations we infer that mantle-derived fluids do not migrate through the seismically defined SAF, but percolate through the eastern fault block.

zone with elevated pore pressure to the NE of the SAF (Zoback *et al.* 2006) and overpressured fluids (∼12 MPa over hydrostatic values at a depth of 1.5 km) were also reported from the Varian-Phillips (VP) well 1.5 km farther to the NE (Johnson & McEvilly 1995). This suggests that the SAF is a barrier for horizontal fluid flow. Recent analyses of noble gas isotopes in 19 mud gas samples from the SAFOD main hole revealed ^{3}He/^{4}He ratios of only ∼0.4 Ra (5 per cent mantle-derived He) on the Pacific Plate and where the borehole intersects the SAF, but up to ∼0.9 Ra (12 per cent mantle) on the North American Plate (Wiersberg & Erzinger 2007). (Ra is the ^{3}He/^{4}He ratio in air. Average values are 8 Ra for mid-ocean ridge basalts (MORB) and 0.02 Ra for the continental crust.) From these observations, we infer that both vertical and horizontal permeability are low within the brittle section of the fault zone. If the seismically defined SAF is largely impermeable, the influx of fluids into this region would be minor, consistent with the geochemical data (Wiersberg & Erzinger 2007). This would explain why intermediate conductivities and not very high conductivities (i.e. when compared with the upper crustal FZC) are observed within the seismogenic zone (*cf.* Figs 11 and 12).

The ^{3}He/^{4}He ratios observed within the SAFOD increase with increasing distance from the borehole into the North American plate (*cf.* Fig. 12c), in good agreement with the much higher ^{3}He/^{4}He ratios of ∼1.6 Ra (∼25 per cent mantle) found in the shallower VP well and Middle-Mountain oil well (Kennedy *et al.* 1997), located 1–1.5 km E of the SAF (*cf.* Fig. 12b). This suggests that the contribution of mantle fluids in the SAFOD borehole is minor when compared to the influx farther to the NE. The geochemical and hydrological data support not only the existence of a channel for deep fluids (i.e. existence of mantle-derived He) but also that its upper branch is offset to the NE of the surface trace of the SAF. Therefore, we interpret the high-conductivity region of the EC as the upper branch of a deep crustal fluid channel, which penetrates into the lower crust and upper mantle. The resistivity model suggests that these fluids pond in the upper crust, bound between the impermeable SAF to the SW and the WCF to the NE. A near-surface stratigraphic or mineralogic seal keeping the fluids overpressured was already suggested by Unsworth & Bedrosian (2004). Some leakage of fluids into the FZC (damage zone of the fault) within the upper 2 km of the fault is plausible.

The source region of mantle fluids seems to be related to the mantle conductor C1 located within the Pacific plate lithosphere and below the Salinian crust. If C1 really is the source region, then any released fluids would have to cross the SAF at lower crustal depths as is implied by the final resistivity models (*cf.* Figs 11 and 12a). Alternatively, fluids could percolate into the North American plate at upper-mantle depths as implied by the resistivity model 1 in Figs 9(a) and (e). This appears to be less likely, however, as it would require a horizontal pressure gradient within the mantle lithosphere driving fluids towards the NE. The potential source region for mantle fluids (C1) is largely located off the profile and, therefore, not well constrained by the available data. If the mantle source region extends as far E as the Sierra Nevada, as discussed by Kennedy *et al.* (1997), then other pathways for fluid ascent may exist. These pathways are not imaged with this profile, but may be linked with a conductive suture zone beneath the eastern Great Valley (Park & Biasi 1991).

A spatial coincidence exists between earthquake locations and the strong resistivity contrast at the E terminus of the Salinian Block. The seismicity observed for this segment of the SAF is confined to the depth range 2–15 km (i.e. directly below the shallow fault zone conductor). The majority of epicentres are located in the

depth range 2–8 km, which coincides with the subvertical resistivity contrast between the resistive Salinian Block basement in the SW and the eastern conductor in the NE. Competing models for the SAF suggested that either a weak (Zoback 2000) or a strong (Scholz 2000) fault is embedded within a strong crust. The resistivity contrast associated with the seismicity likely reflects a change in the rheology, from the strong Salinian Block basement in the SW to presumably much weaker, reworked Franciscan complex or sedimentary rocks to the NE that may contain overpressured fluids. The resistivity model gives the impression that the crust is strong to the SW of the SAF and weak to the NE. This setting could be an important factor in controlling the present location of the SAF.

This does not, however, imply that no strain is accommodated within the fluidized region between the SAF and the WCF, where pore pressures appear to be high. We assume that in this region, compressional strain is accommodated by blind thrusting (Miller 1996) and hence appears effectively seismically quiet.

5 CONCLUSIONS

MT data along a 45 km long profile across the SAF near the SAFOD was used to derive a crustal electrical resistivity model. Data analysis revealed that the majority of the data are consistent with 2-D modelling assumptions. The dominant geoelectrical strike direction is N42.5°E in agreement with the strike of the SAF and other major geological units in the region.

A 2-D resistivity cross-section was obtained from smoothing regularized inversion. The final resistivity model (Fig. 11) reveals an image of a heterogeneous upper crust with a number of conductive and resistive anomalies that are related to the sedimentary sequences, the Franciscan subduction complex and blocks of Salinian crust forming the basement to the NE and SW of the SAF, respectively. The most intriguing feature of the regional electrical resistivity model is an approximately 5–8 km wide, subvertical corridor of high electrical conductivity (EC) in the upper crust that widens in the lower crust (LCZ). The zone of high conductivity reaches the near-surface 5–10 km NE of the SAF and is subhorizontally connected with the FZC at the SAF. Low resistivities of less than 5 Ωm are imaged within the EC to a depth of 8–10 km adjacent to the SAF. From there, the anomaly appears to link with a lower crustal high conductivity zone (LCZ) at non-seismogenic depths (>12–15 km). Constrained inversions (Fig. 9) show that neither the upper branch of the high-conductivity zone (EC) nor its LCZ can be removed without significantly increasing data misfit.

A joint interpretation of the resistivity structure and the geochemical data from the SAFOD and nearby water wells suggests that the crust near the SAF provides pathways for crustal and upper-mantle fluids, while the eastern fault block represents a trap of fluids. This interpretation is supported by (i) increasing $^3He/^4He$ ratios within the SAFOD (up to 11 per cent mantle derived) to the NE of the SAF (Wiersberg & Erzinger 2007) (ii) high $^3He/^4He$ ratios farther to the NE (up to 25 per cent mantle), observed within the VP and Middle Mountain oil wells (Kennedy *et al.* 1997) (iii) an electrically conductive channel linking the upper crustal eastern conductor (EC) with a lower crustal conductive zone and a conductive anomaly within the upper mantle. Furthermore, superhydrostatic fluid pressures within the SAFOD to the NE of the SAF (Zoback *et al.* 2006) as well as within the VP well (Johnson & McEvilly 1995) suggest that the EC represents a region of overpressured fluids trapped between an impermeable SAF, the WCF and below a surficial seal. Elevated fluid pressures in this region could be related to continuous or episodical fluid supply of deep rooted fluids.

Within the upper crust, these fluids do not migrate through the seismically defined SAF. Instead, upper crustal migration pathways are provided within the high-conductivity EC sandwiched between the SAF and a SW-dipping segment of the WCF, interpreted to represent a thrust-fault penetrating at least to the bottom of the seismogenic zone (Carena 2006). Seismically active as well as blind thrust-faults in this region could also provide the means for fracture-related fluid-flow, in agreement with the modelling assumption of Miller (1996).

High lower crustal conductivities within a 25 km wide zone around the SAF indicate anomalously high fluid content. Constrained inversion shows that a lower crustal barrier for fluid flow is incompatible with the MT data. The resistivity model strongly supports deep fluid circulation and migration through the lower crust. The exact geometry of these deep pathways can not be resolved. However, inversion models containing a narrow, steeply dipping conductive zone as an *a priori* conductive structure achieve the best data fit, and seem to support the existence of a narrow pathway.

We speculate that the source region for the fluids is related to a mantle conductivity anomaly below the Pacific plate. This mantle anomaly could be related to fluids released from a subducted slab of oceanic crust, which may exist in this region (Zoback 2002). However, a longer MT profile extending to the coast and continued off-shore is required to constrain this feature.

Further geochemical sampling of water wells along the MT profile would be necessary to test if elevated mantle gas content exists between the SAF and the WCF as predicted by the MT model. Farther to the NE, mantle derived fluids should be minor constituents to the fluid composition, similar to the observations to the SW of the SAF.

The resistivity model in Fig. 11 may have important implications for the occurrence of the recently observed non-volcanic tremors beneath the SAF near Cholame (Nadeau & Dolenc 2005), approximately 40 km SE of Parkfield. Near Cholame, earlier MT work found evidence for a resistive crust at depths of 40 km beneath the SAF (Park & Biasi 1991) which could be indicative of a dry zone capable of trapping fluids below. The situation near Cholame seems to be markedly different from Parkfield (this study), where the resistivity model and the fluid chemistry (Kennedy *et al.* 1997; Wiersberg & Erzinger 2007) suggest a pathway for fluids into the brittle regime of the SAF system. This would be consistent with low mantle derived He content in the Jack-Ranch Highway-46 Well (Kennedy *et al.* 1997) near Cholame and in support of a locally well-confined source region for the non-volcanic tremors (Nadeau & Dolenc 2005). We speculate that this along-strike variability between Parkfield and Cholame is related to the transition from a seismically creeping to a locked segment of the SAF and thereby directly to earthquake generation processes.

ACKNOWLEDGMENTS

MT data from M. Unsworth from previous experiments are gratefully acknowledged. Instruments for the experiments were provided by the Geophysical Instrument Pool Potsdam (GIPP) and by the Electromagnetic Studies of the Continents (EMSOC) facility. We would like to express our sincere thanks to Paul Brophy for his tireless support in logistic matters and to the landowners for permitting us access to their properties. This work was funded by the Deutsche Forschungsgemeinschaft (DFG, Ri-1127/2) and the National Science Foundation (NSF, NSF0454283). We are grateful to the referees (C. G. Farquharson and an anonymous one) and the

Editor, T. Minshull, for their constructive comments that helped to clarify the manuscript.

REFERENCES

Bahr, K., 1988. Interpretation of the magnetotelluric impedance tensor: regional induction and local telluric distortion, *J. Geophys.,* **62,** 119–127.

Becken, M. & Burkhardt, H., 2004. An ellipticity criterion in magnetotelluric tensor analysis, *Geophys. J. Int.,* **159,** 69–82.

Becken, M., Ritter, O. & Burkhardt, H., 2008. Mode separation of magnetotelluric responses in three-dimensional environments, *Geophys. J. Int.,* **172,** 67–86.

Bedrosian, P.A., Unsworth, M.J., Egbert, G.D. & Thurber, C.H., 2004. Geophysical images of the creeping segment of the San Andreas fault: implications for the role of crustal fluids in the earthquake process., *Tectonophysics,* **385,** 137–156.

Bleibinhaus, F., Hole, J.A., Ryberg, T. & Fuis, G.S., 2007. Structure of the California Coast Ranges and San Andreas Fault at SAFOD from seismic waveform inversion and reflection imaging, *J. geophys. Res.,* **112,** B06315.

Booker, J.R., Favetto, A. & Pomposiello, M.C., 2005. Low electrical resistivity associated with plunging of the Nazca flat slab beneath Argentina, *Nature,* **429,** 399–403.

Buske, S., Gutjahr, S., Rentsch, S. & Shapiro, S., 2006. Active and Passive Seismic Imaging of the San-Andreas-Fault-System, *AGU Fall Meeting Abstracts,* pp. A485.

Caldwell, T.G., Bibby, H.M. & Brown, C., 2004. The magnetotelluric phase tensor, *Geophys. J. Int.,* **158,** 457–469.

Carena, S., 2006. 3-D Geometry of Active Deformation East of the San Andreas Fault Near Parkfield, California, *AGU Fall Meeting Abstracts,* pp. C178.

Diblee, T.W., 1972. Geologic maps of fourteen 15-minute quadrangles along the San Andreas Fault in the vicinity of Paso Robles and Cholame southeastward to Maricopa and Cuyama, California, Tech. Rep. 99, US. Geol. Surv. Open File Rep.

Egbert, G.D. & Booker, J.R., 1986. Robust estimation of geomagnetic transfer functions, *Geophys. J. R. astr. Soc.,* **87,** 173–194.

Groom, R.W. & Bailey, R.C., 1989. Decomposition of magnetotelluric impedance tensors in presence of local three-dimensional galvanic distortion, *J. geophys. Res.,* **94,** 1913–1925.

Gueguen, Y. & Palciauskas, V., 1994. *Introduction to the Physics of Rocks,* Princeton University Press, Princeton, NJ.

Guzofski, C.A., Shaw, J.H., Lin, G. & Shearer, P.M., 2007. Seismically active wedge structure beneath the Coalinga anticline, San Joaquin basin, California, *J. geophys. Res.,* **112,** B03S05.

Hardebeck, J.L. & Hauksson, E., 1999. Role of Fluids in Faulting Inferred from Stress Field Signatures, *Science,* **285,** 236–239.

Hickman, S., Zoback, M. & Ellsworth, W., 2004. Introduction to special section: preparing for the San Andreas Fault Observatory at Depth, *Geophys. Res. Lett.,* **31,** L12S01.

Hole, J.A., Ryberg, T., Fuis, G.S., Bleibinhaus, F. & Sharma, A.K., 2006. Structure of the San Andreas Fault at SAFOD from a seismic refraction survey, *Geophys. Res. Lett.,* **33,** L02712.

Johnson, P.A. & McEvilly, T.V., 1995. Parkfield seismicity: fluid-driven, *J. geophys. Res.,* **100,** 12 937–12 950.

Jones, A., 1992. Electrical conductivity of the continental lower crust, in *Continental Lower Crust,* pp. 81–143, eds Fountain, D., Arculus, R. & Kay, R., Elsevier, Amsterdam.

Kennedy, B.M., Kharake, Y.K., Evans, W.C., Ellwood, A., DePaolo, D.J., Thordsen, J. & Mariner, R.H., 1997. Mantle Fluids in the San Andreas Fault System, California, *Science,* **278,** 1278–1281.

Mackie, R.L., Bennet, B.R. & Madden, T.R., 1988. Long-period magnetotelluric measurements near the central California coast: a land-locked view of the conductivity structure under the Pacific Ocean, *Geophys. J. Int.,* **95,** 181–194.

Madden, T.R., 1972. Transmission systems and network analogies to geophysical forward and inverse problems, Report No. 72-3, Dept. of Geology and Geophysics, MIT, Cambridge, MA.

McNeice, G.W. & Jones, A.G., 2001. Multi-site, multi-frequency tensor decomposition of magnetotelluric data, *Geophysics,* **66,** 158–173.

McPhee, D.K., Jachens, R.C. & Wentworth, C.M., 2004. Crustal structure across the San Andreas Fault at the SAFOD site from potential field and geologic studies, *Geophys. Res. Lett.,* **31,** L12S03.

Miller, S.A., 1996. Fluid-mediated influence of adjacent thrusting on the seismic cycle at Parkfield, *Nature,* **382,** 799–802.

Nadeau, R.M. & Dolenc, D., 2005. Nonvolcanic Tremors Deep Beneath the San Andreas Fault, *Science,* **21,** 389.

Park, S.K. & Biasi, G.P., 1991. Magnetotellric Evidence for Crustal Suture Zones Bounding the Southern Great Valley, California, *J. geophys. Res.,* **96,** 14 211–14 237.

Ritter, O., Junge, A. & Dawes, G.J.K., 1998. New equipment and processing for magnetotelluric remote reference observations, *Geophys. J. Int.,* **132,** 535–548.

Ritter, O., Hoffmann-Rothe, A., Bedrosian, P.A., Weckmann, U. & Haak, V., 2005. Electrical conductivity images of active and fossil fault zones, in *High-Strain Zones: Structure and Physical Properties,* Vol. 245, pp. 165–186, eds Bruhn, D. & Burlini, L., Geological Society of London Special Publications.

Roberts, C.W. & Jachens, R.C., 1999. Preliminary aeromagnetic anomaly map of California, Tech. Rep.99, US. Geol. Surv. Open File Rep.

Rodi, W. & Mackie, R.L., 2001. Nonlinear conjugate gradients algorithm for 2-D magnetotelluric inversions, *Geophysics,* **66,** 174–187.

Ryberg, T., Fuis, G.S., Bauer, K., Hole, J.A. & Bleibinhaus, F., 2005. Upper-Crustal Reflectivity of the Central California Coast Range Near the San Andreas Fault Observatory at Depth (SAFOD), USA, *AGU Fall Meeting Abstracts,* pp. A441.

Scholz, C.H., 2000. Evidence for a strong San Andreas Fault, *Geology,* **28,** 163–166.

Smith, J.T., 1995. Understanding telluric distortion matrices, *Geophys. J. Int.,* **122,** 219–226.

Thurber, C., Zhang, H., Waldhauser, F., Hardebeck, J., Michael, A. & Eberhart-Phillips, D., 2006. Three-dimensional compressional wavespeed model, earthquake relocations, and focal mechanisms for the Parkfield, California, region, *Bull. seism. Soc. Am.,* **96,** S38–S49.

Unsworth, M.J. & Bedrosian, P., 2004. Electrical Resistivity structure at the SAFOD site from magnetotelluiric exploration, *Geophys. Res. Lett.,* **31,** L12S05.

Unsworth, M.J., Malin, P.E., Egbert, G.D. & Booker, J.R., 1997. Internal structure of the San Andreas fault at Parkfield, California, *Geology,* **25,** 359–362.

Unsworth, M.J., Egbert, G.D. & Booker, J.R., 1999. High resolution electromagnetic imaging of the San Andreas Fault in Central California, *J. geophys. Res.,* **104,** 1131–1150.

Unsworth, M.J., Bedrosian, P., Eisel, M., Egbert, G.D. & Siripunvaraporn, W., 2000. Along strike variations in the electrical structure of the San Andreas Fault at Parkfield, California., *Geophys. Res. Lett.,* **27,** 3021–3024.

Wannamaker, P.E., 1999. Affordable magnetotellurics: interpretation in natural environments, in *Three-Dimensional Electromagnetics,* pp. 349–374, eds Oristaglio, M. & Spies, B., SEG, Tulsa.

Weckmann, U., Magunia, A. & Ritter, O., 2005. Effective noise separation for magnetotelluric single site data processing using a frequency domain selection scheme, *Geophys. J. Int.,* **162**(3), 635–652.

Wiersberg, T. & Erzinger, J., 2007. A helium isotope cross-section study through the San Andreas Fault at seismogenic depths, *Geochem. Geophys. Geosyst.,* **8,** Q01002.

Wiese, H., 1962. Geomagnetische Tiefentellurik Teil ii: Die Streichrichtung der Untergrundstrukturen des elektrischen Widerstandes, erschlossen aus geomagnetischen Variationen, *Geofis. Pura e Appl.,* **52,** 83–103.

Zoback, M., 2000. Strength of the San Andreas, *Nature,* **44,** 31–32.

Zoback, M., 2002. Steady-state failure equilibrium and deformation of intraplate lithosphere, *Int. Geol. Rev.,* **44,** 383–401.

Zoback, M., Hickman, S. & Ellsworth, W., 2006. Structure and properties of the San Andreas fault in central California: preliminary results from the SAFOD experiment, in *Geophys. Res. Abstracts,* Vol. 8, EGU.